Available online at www.ijournalse.org

Emerging Science Journal

(ISSN: 2610-9182)

Vol. 7, No. 4, August, 2023

Multi-Fusion Algorithms for Detecting Land Surface Pattern Changes Using Multi-High Spatial Resolution Images and Remote Sensing Analysis

Hayder Dibs [1], Hussein Sabah Jaber [2], Nadhir Al-Ansari [3*]

[1] *Water Resources Management Engineering Department, Faculty of Engineering, Al-Qasim Green University, Babylon, 51001, Iraq.*

[2] *Department of Surveying, College of Engineering, University of Baghdad, Baghdad, Iraq.*

[3] *Department of Civil Environmental and Natural Resources Engineering, Lulea University of Technology, 971 87 Lulea, Sweden.*

Abstract

Producing accurate Land-Use and Land-Cover (LU/LC) maps using low-spatial-resolution images is a difficult task. Pan-sharpening is crucial for estimating LU/LC patterns. This study aimed to identify the most precise procedure for estimating LU/LC by adopting two fusion approaches, namely Color Normalized Brovey (BM) and Gram-Schmidt Spectral Sharpening (GS), on high-spatial-resolution Multi-sensor and Multi-spectral images, such as (1) the Unmanned Aerial Vehicle (UAV) system, (2) the WorldView-2 satellite system, and (3) low-spatial-resolution images like the Sentinel-2 satellite, to generate six levels of fused images with the three original multi-spectral images. The Maximum Likelihood method (ML) was used for classifying all nine images. A confusion matrix was used to evaluate the accuracy of each single classified image. The obtained results were statistically compared to determine the most reliable, accurate, and appropriate LU/LC map and procedure. It was found that applying GS to the fused image, which integrated WorldView-2 and Sentinel-2 satellite images and was classified by the ML method, produced the most accurate results. This procedure has an overall accuracy of 88.47% and a kappa coefficient of 0.85. However, the overall accuracies of the three classified multispectral images range between 86.84% to 76.49%. Furthermore, the accuracy assessment of the fused images by the Brovey method and the rest of the GS method and classified by the ML method ranges between 85.75% to 76.68%. This proposed procedure shows a lot of promise in the academic sphere for mapping LU/LC. Previous researchers have mostly used satellite images or datasets with similar spatial and spectral resolution, at least for tropical areas like the study area of this research, to detect land surface patterns. However, no one has previously investigated and examined the use and application of different datasets that have different spectral and spatial resolutions and their accuracy for mapping LU/LC. This study has successfully adopted different datasets provided by different sensors with varying spectral and spatial levels to investigate this.

Keywords:
Image Fusion;
Brovey Method;
Gram-Schmidt Approach;
Image Classification;
LU/LC.

Article History:

Received:	23	February	2023
Revised:	17	June	2023
Accepted:	03	July	2023
Available online:	12	July	2023

1- Introduction

Obtaining an accurate Land-Use and Land-Cover (LU/LC) thematic map through image classification is crucial in many remote sensing applications, such as detecting climate changes, monitoring and managing the environment, and tracking hazards and urbanization expansion [1–5]. The selection of a reliable classifier approach is essential to achieving an accurate estimation of the LU/LC thematic map [6, 7]. There are various approaches and methodologies available for predicting the LU/LC maps, including pixel-based classifiers and object-based methods such as Decision Trees (DT), Artificial Neural Network (ANN), Support Vector Machine (SVM), and Spectral Angle Mapper (SAM) algorithms, as

* **CONTACT**: nadhir.alansari@ltu.se

DOI: http://dx.doi.org/10.28991/ESJ-2023-07-04-013

referenced by [8–10]. Additionally, various improved approaches have been adopted to enhance the LU/LC estimation, such as imagery spectral pan-sharpening algorithms [11, 12]. To perform any image classification, several stages need to be completed, including (1) selection of training sites based on visual image interpretation techniques; (2) selection of testing samples based on fieldwork or other techniques; (3) preprocessing steps such as geometric, atmospheric, and radiometric corrections; (4) object extraction; (5) selection of a classifier approach; (6) post-classification; and (7) result validation [7, 13, 14].

Remote sensing is a broad strategy for extracting knowledge about the Earth's structure and composition by gathering and analyzing objects from considerable distances [15]. Researchers and analysts propose different techniques and methods to estimate an accurate map of LU/LC. For example, using spectral indexes is one of the methods that have been widely adopted in imagery classification of both low, medium, and high spectral and spatial resolutions of remotely sensed datasets, such as Vegetation Indexes [16, 17], Water Index [18–20], normalized-difference building index [16], ecological-index [17], normalized-difference vegetation index [17, 21], and derivative indices, e.g., the re-normalized-difference vegetation index [17, 22], a growing-season-normalized-difference-vegetation-index [23, 24]. Short periods of each low, medium, and high spectral and spatial-resolution imagery have several advantages, and several analysts have adopted Spectral-Indices to a Time-Series-Image [18, 25, 26]. Indices are commonly used to reflect LU/LC information throughout a simple band calculation [14].

Image fusion is one solution to overcome the low spatial resolution of remote sensing datasets dilemma. Indeed, satellite systems such as Ikonos, QuickBird, and Worldview sensors can supply images with only panchromatic imagery that has a high spatial resolution, but they also provide images that have a low multi-spectral resolution [27]. The Pan-sharpening method is one of the special cases of image fusion. It is capable of providing images with high resolutions (spatial and spectral). Moreover, pan-sharpening methods provide fused images with a spectral response that is the same as that of the Multi-Spectral images and with the same panchromatic resolution. The pan-sharpened images have great potential for different kinds of applications such as LU/LC cover, land classification, LU/LC change detection, and environment management [28, 29].

In general, pan-sharpening algorithms can be categorized into three types: (1) Component Substitution Algorithms (SA), (2) Multi-Resolution Analysis approaches (MRA), and (3) Model-Based methods. Additionally, there are several other sub-categories of pan-sharpening techniques as reported by Li et al. [30]. Specifically, SA approaches such as intensity-hue-saturation (IHS) [31], the GS algorithm referenced by Laben and Brower [32], and Principle Component Analysis [33] work by separating components into color space using spectral transform techniques like IHS or GS. Then, a panchromatic image is used to substitute the component with sufficient spatial details to improve spatial resolution. In the end, the pan-sharpened multi-spectral images are obtained by inverting the spectral transform. On the other hand, MRA techniques usually use digital filters to cover wavelet-transform [34], contourlet-transform [35], curvelet-transform [36], Laplacian-pyramids [7], and ripplet-transform [15] for obtaining a multi-scale representation of the spectral imagery. MRA works by first applying MRA transforms to decompose the panchromatic imagery into multi-scale components. Then, an equivalent spatial information has high-frequency components injected into an upsampled spectral imagery. The MRA and SA details are reported by Aiazzi et al. [37].

Furthermore, integration is often made between MRA transforms and edge-preserving filters [38]. The third class, known as model-based methods, includes compressed sensing-based methods (CSBMs) [15, 39] and sparse matrix factorization technique-based approaches (SMFTBAs) [40]. The compressed-sensing-based algorithm conducts spectral sharpening by reconstructing highly resolved spectral imagery using extracted imagery patches from the sources of panchromatic and multi-spectral imagery. The SA methods can enhance the spatial resolution of spectral imagery while having high efficiency and convenience for conducting such tasks, such as the IHS method [41]. When comparing SA and MRA methods, the latter achieves superior spectral fidelity (SSF), although spatial resolution improvement will be limited. In previous works, most researchers applied satellite images or datasets with the same spatial and spectral resolution, at least in a tropical area like the study area of this research, to detect land surface patterns. However, no one has investigated and examined the use and application of different datasets with varying spectral and spatial resolutions and checked the accuracy of the obtained results, whether high or low. In this study, different datasets provided by different sensors with varying spectral and spatial levels were adopted. In previous works, most researchers applied satellite images or datasets with the same spatial and spectral resolution to at least a tropical area, such as the study area of this research, to detect land surface patterns [17–21]. No one investigates and examines using and applying different datasets with different spectral and spatial resolutions to do so and checks the accuracy of the obtained results if it is high either low. In this study, it is adopted different datasets provided by different sensors have different in their images in spectral and spatial levels.

Many pan-sharpening algorithms and techniques can be applied to different remote sensing images. However, there are some questions that need to be answered: (1) Will incorporating high spatial resolution images into image classification analysis improve the accuracy of the obtained thematic map for estimating the LU/LC map? (2) Which datasets are the best among the UAV, WorldView-2, and Sentinel-2 images for estimating the LU/LC? (3) What is the best pan-sharpening algorithm to improve and enhance the obtained LU/LC? To find out the answers to all these

questions, the current study investigates pan-sharpening methods on the three multispectral images and the fused images of the UAV, WorldView-2, and Sentinel-2 images. The results will be examined using the ML method of a pixel-based classification approach to propose the estimation of LU/LC. The research outcomes will make important contributions to academia and improve and enhance the present study for use with different datasets, applications, sources, and sites.

2- Methods and Data Analysis

In this research, a variety of multi-sensor and multi-spectral images were utilized. Before processing and analysis, the images were corrected for radiometric and geometric noise and underwent image registration and resampling. The study area was then extracted from the images to streamline dataset processing. Two methods of image fusion were used to produce six levels of fused images from the aerial and satellite images. An image classification algorithm was then applied to the nine images to estimate the land use/land cover types for the study area. The accuracy of the results was evaluated using a confusion matrix method to determine the most precise procedure for mapping the land use/land cover map for the small-scale area. The methodology is illustrated in Figure 1.

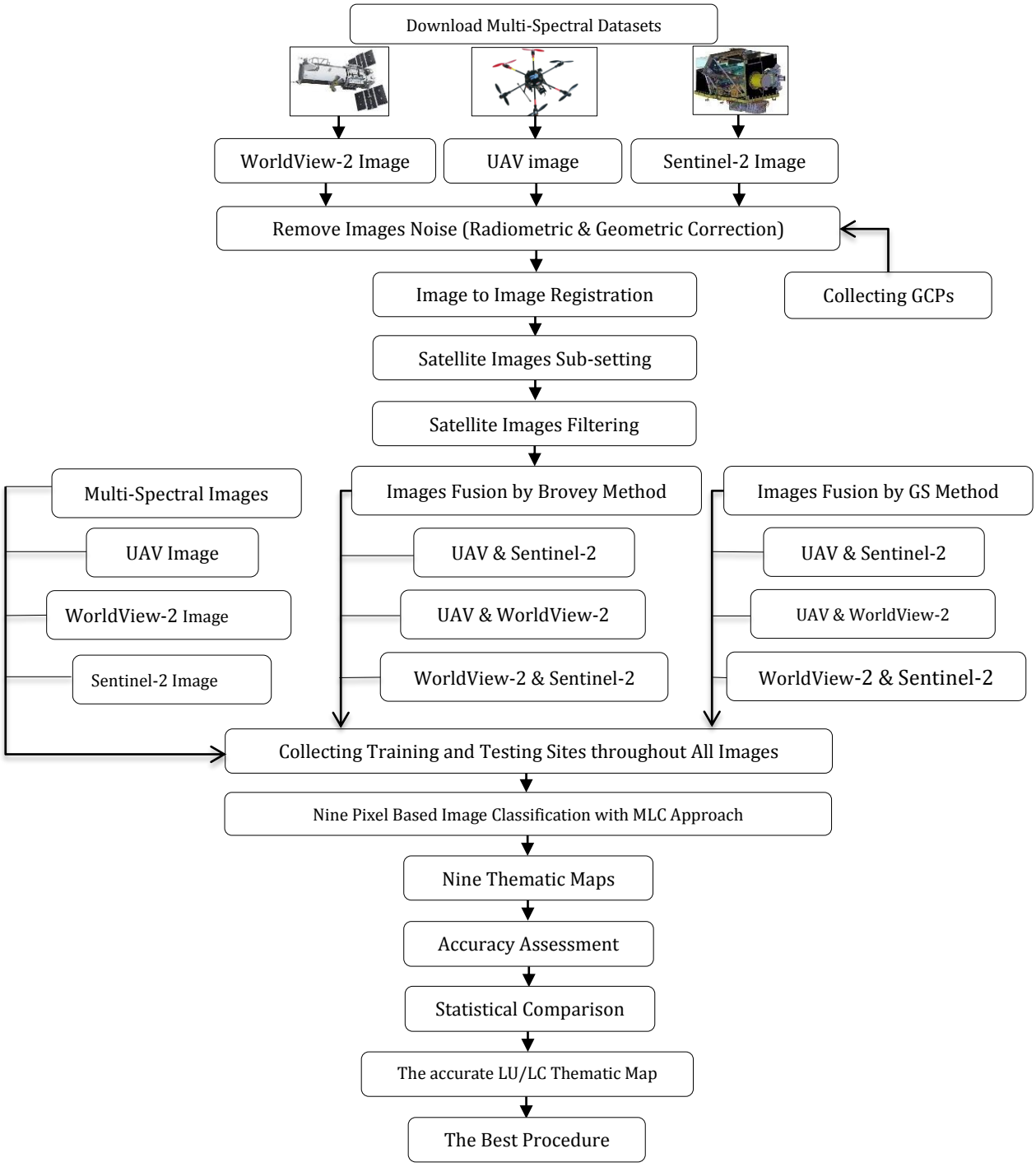

Figure 1. The flowchart of the methodology

2-1- The Study Area Site Description

The study area selected for this research includes the small-scale area of the Faculty of Engineering, University of Putra Malaysia (UPM), and the neighboring district. This area is located in Serdang, Selangor State, Malaysia. UPM is well-known as a Malaysian research university that was established with the Faculty of Agricultural Sciences, and since 1997, it has expanded to open many scientific research centers, educational institutions, and faculties. The study area is located between the coordinates of 03° 00'39.21"N - 03° 00'16.01"N and 101°42'53.57"E - 101°43'30.89"E, as shown in Figure 2, which illustrates the location of the Faculty of Engineering. Like other cities in peninsular Malaysia, the study area has a tropical rainforest climate with consistent temperatures ranging from 23.2°C to 31.9°C throughout the year, heavy rains during November, and a humid atmosphere [9]. Figure 3 shows the climate datasets for temperature and precipitation in the study area.

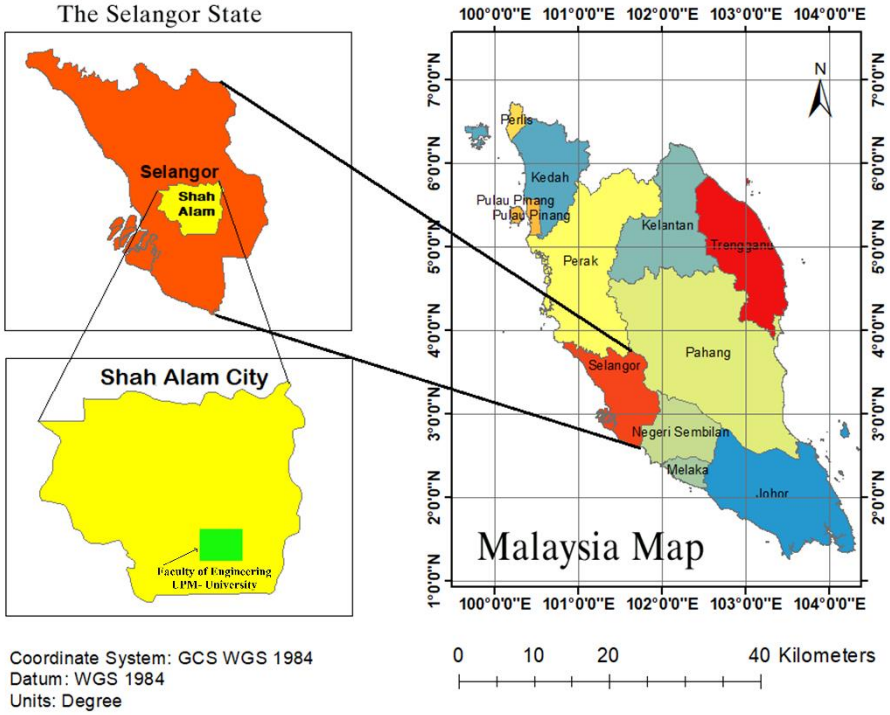

Figure 2. Study Area location in the UPM and the neighbor district, Selangor, Malaysia

Climate data for Klang, Malaysia (Approximation 7km distance from Shah Alam) [hide]													
Month	Jan	Feb	Mar	Apr	May	Jun	Jul	Aug	Sep	Oct	Nov	Dec	Year
Average high °C (°F)	32 (90)	32 (90)	33 (91)	32 (90)	32 (90)	32 (90)	32 (90)	32 (90)	32 (90)	32 (90)	31 (88)	31 (88)	32 (90)
Daily mean °C (°F)	27 (81)	28 (82)	28 (82)	28 (82)	28 (82)	28 (82)	28 (82)	28 (82)	28 (82)	28 (82)	27 (81)	27 (81)	28 (82)
Average low °C (°F)	23 (73)	23 (73)	23 (73)	24 (75)	24 (75)	23 (73)	23 (73)	23 (73)	23 (73)	23 (73)	23 (73)	23 (73)	23 (73)
Average precipitation mm (inches)	162.6 (6.40)	170.2 (6.70)	231.1 (9.10)	276.9 (10.90)	195.6 (7.70)	124.5 (4.90)	127.0 (5.00)	142.2 (5.60)	195.6 (7.70)	266.7 (10.50)	281.9 (11.10)	228.6 (9.00)	2,402.9 (94.6)
Source: The Weather Channel Forecasts[8]													

Figure 3. Indicates the study area climate data of temperatures and precipitations

2-2- The Satellite and Aerial Images

Satellite and aerial images were utilized for this study, which were obtained from different remote sensing sensors such as WorldView-2, Sentinel-2 satellite systems, and the UAV sensor. All details, capture dates, and information about the applied datasets in this research are indicated as follows. The first image used in the study was obtained from the UAV sensor. The UAV image covered the Faculty of Engineering at UPM University and the nearest district, and it was acquired on February 3, 2017 (Figure 4). The captured image was obtained using a Multi-rotor UAV flying at an altitude of about 328m above the ground surface using a Canon Power Shot (SX230 HS), which is capable of capturing an image with 12.1 Mega-pixels. The image was characterized by three bands (RGB) with a ground resolution of approximately 9.95 cm/pixel and a pixel resolution of 4000 x 3000. The image has a ground coverage area of about 1.50 km^2, with around 60% as a forward overlap. The captured UAV imagery for this study is shown in Figure 4.

Figure 4. the UAV image of the Faculty of Engineering of the study area

The second set of data used in this study was obtained from the WorldView-2 Satellite system, with a spatial resolution of 0.50m. The WorldView-2 satellite was launched into space in 2009 by the Digital Globe Company. It orbits at an inclination of about 97.2° with an altitude of 770km, completing one cycle every 100 minutes. The swath width of this sensor at its nadir is 16.4 km. The WorldView-2 has two push-broom sensors that provide images with Panchromatic and Multi-Spectral bands [42]. The former has a spatial resolution of about 0.50m, but it is resampled to 0.50m for commercial use. Its spectral interval ranges between 0.450µm and 0.800µm. The Multi-Spectral image has a spatial resolution of about 1.85m, which is resampled to 2m for commercial use. The WorldView-2 sensor acquires 8 bands: Coastal (0.400µm–0.450µm), Blue (0.450µm–0.510µm), Green (0.510µm–0.580µm), Yellow (0.585µm–0.625µm), Red (0.630µm–0.690µm), Red-Edge (0.705µm–0.745µm), Near-IR1 (0.770µm–0.895µm), and Near-IR2 (0.860µm–1.04µm) [42]. In this study, the WorldView-2 image captured the Faculty of Engineering at UPM University and the surrounding district in Serdang, Selangor, Malaysia. The dataset was acquired on February 3, 2019, and is georeferenced in the UTM with WGS-84 as a datum (Figure 5).

Figure 5. the WorldView-2 image of the study area, Malaysia

The third set of data used in this research was obtained from the Sentinel-2 satellite image. Sentinel-2 is a European wide-swath, high-spatial-resolution satellite with a multi-spectral band. Its full mission has specifications for twin

satellite systems flying together in the same orbit. It is designed to complete one cycle around the Earth in about 5 days at the equator. Sentinel-2 has an optical instrument with 13 bands: four bands with a spatial resolution of 10 m, six bands with (20m), and other bands with a spatial resolution of (60m). The Sentinel-2 has a swath width of (290km), and its images have different applications in remote sensing and GIS. The Sentinel-2 image used in this study was acquired over the University Putra Malaysia campus, Faculty of Engineering, on February 3, 2019 (Figure 6).

Figure 6. the Sentinel-2 image of the Faculty of Engineering, UPM University, Malaysia

3- Image Noise Removal

In this stage of the research, image pre-processing was performed to reduce and remove the image noise that was obtained during the capture. These corrections included geometric and radiometric corrections, as well as image-to-image registration. Envi software was used to perform all of these corrections. Correcting geometric noise is important for any remotely sensed imagery, and it should be done before proceeding to further processing and analysis [1]. The most important step in performing geometric correction is the selection of Ground Control Points (GCPs) locations. For this study, 14 GCPs were collected and distributed evenly throughout the UAV imagery portions. The selection of GCPs was performed using the Google Earth Pro-Environment, as well as the visual interpretation of the study area UAV image in the Faculty of Engineering, Malaysia, as indicated in Table 1 and Figure 7. The first polynomial transformation was used to correct the geometric noise of this image, and the nearest-neighbor-method (NNM) was applied to calculate a Root-Mean-Square-Error (RMSE), which was found to be equal to 1.17 pixels.

Table 1. the 14 GCPs coordinates

No.	Latitude	Longitude
1	3° 00'40.40"N	101°43'23.57"E
2	3° 00'41.03"N	101°43'06.01"E
3	3° 00'36.29"N	101°43'09.43"E
4	3° 00'41.04"N	101°42'55.82"E
5	3° 00'17.07"N	101°42'54.90"E
6	3° 00'26.79"N	101°43'19.64"E
7	3° 00'28.06"N	101°42'55.03"E
8	3° 00'36.35"N	101°42'59.05"E
9	3° 00'34.31"N	101°43'24.49"E
10	3° 00'29.34"N	101°43'11.75"E
11	3° 00'16.71"N	101°43'02.14"E
12	3° 00'17.41"N	101°43'10.26"E
13	3° 00'20.34"N	101°43'17.48"E
14	3° 00'25.69"N	101°43'02.63"E

Figure 7. the collected 14-GCPs throughout the study area

The next step was to perform image registration for the Sentinel-2 and WorldView-2 images. This was done by considering the UAV image as the reference image and the other two images as slaves. The image-to-image technique was used to register the reference and slave images. Figure 8 illustrates the image-to-image registration process performed between the reference and slave images.

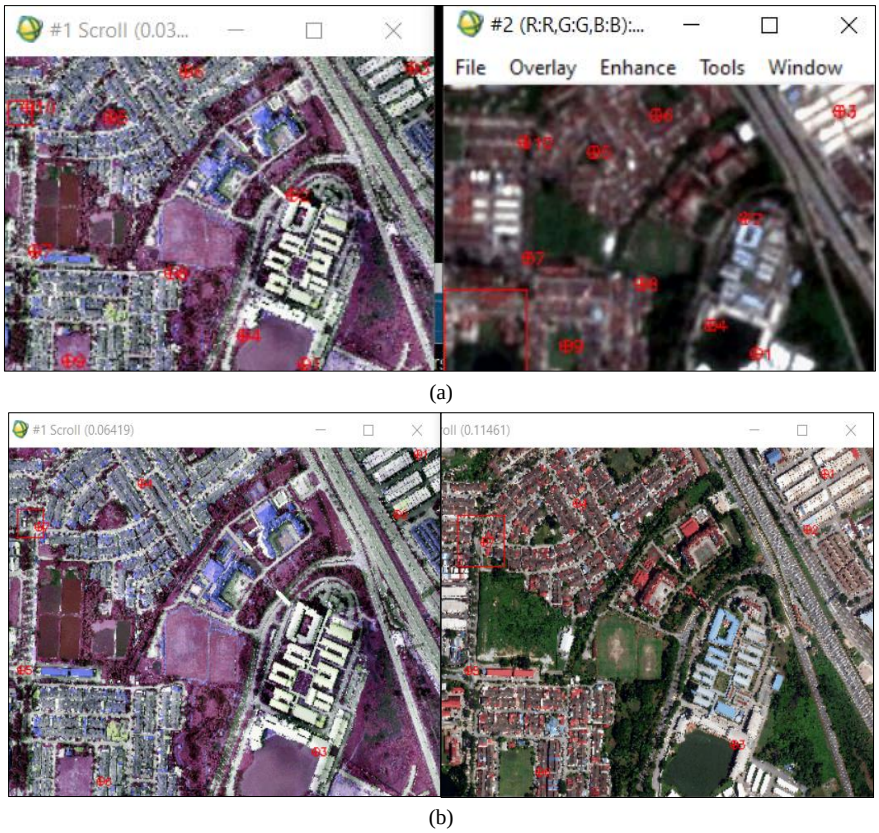

Figure 8. (a) the UAV and Sentinel-2 images registration and (b) UAV and WorldView-2 images registration

The next correction method for the utilized images was the removal of radiometric noise. This is an essential step in digital imagery to eliminate the effects of the atmosphere and sun illumination [2, 16]. The dark-object subtraction (DOS) was selected to remove the radiance error from all data: UAV, WorldView-2, and Sentinel-2 images. Figure 9 illustrates the final corrected images with all noise types removed. Then, in the processing step, image layer stacking, image subsetting, and image filtering were performed to make all datasets ready for further processing and analysis and to save processing time and storage.

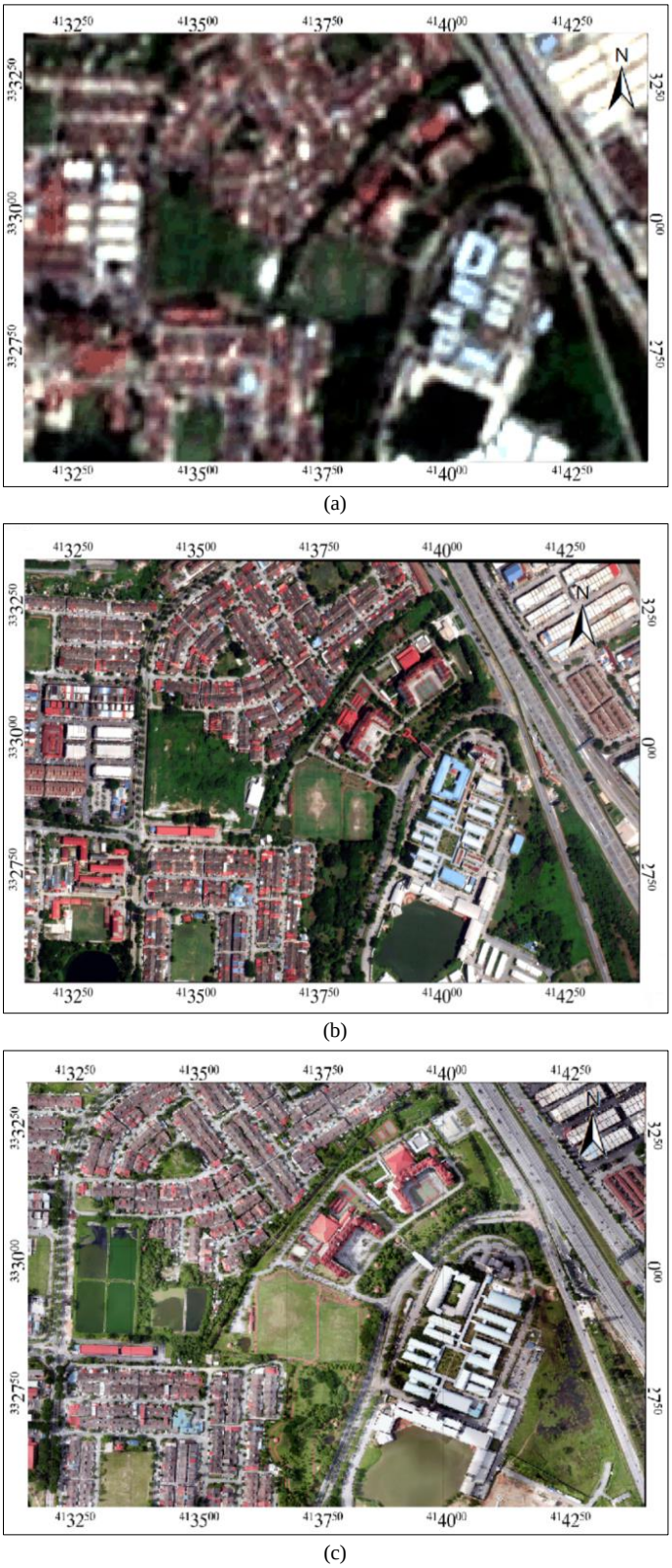

(a)

(b)

(c)

Figure 9. corrected images after removing all noises. (A) Sentinel-2 image, (B) WorldView-2 image, (C) UAV image

4- Pan-Sharpening Image Algorithms

In this research, after finishing the application of image layer stacking, area sub-setting, and imagery filtering, the three Multi-Spectral images were integrated and fused using two different spectral sharpening approaches. The first level of fusion was done using the Brovey method between the UAV image and each of the WorldView-2 and Sentinel-2 images. The UAV image is considered the reference image in image fusion processing because it is the highest-resolution image, and both the WorldView-2 and Sentinel-2 images are considered as slave images. The Brovey pan-sharpening technique uses a mathematical combination for integrating different spatial resolution (high and low) bands, as reported

by Vrabel [43]. For this approach, each multispectral imagery is multiplied by the ratio of a high-resolution band and then divided by the multispectral image. The Brovey transform was invented by American scientists to increase the visual contrast at the low and high ends of the image histogram [44]. The Brovey approach is an arithmetic operation combination that requires spectral band normalization before performing multiplication by the high-resolution image or band. The Brovey approach may lead to color distortion [45]. The outcome of the processing will automatically resample the multispectral bands to the high-resolution image pixel size [46]. The fused channels of the R, G, and B image bands (MSout) are explained in detail in the equations below [47]. The result of the RGB image will have the same input high-resolution band pixel size. The Brovey approach equations are:

$$\mathrm{MS_{out}} = \frac{\mathrm{MS_i}}{\mathrm{MS_{tot}}} \,.\, \mathrm{HRI} \tag{1}$$

where, $\mathrm{MS_i}$, is the {i-th}spectral band, $\mathrm{MS_{tot}}$, is the combination of the spectral bands, $\mathrm{MS_{tot}}$ calculates by the following equations [47]:

$$\mathrm{MS_{tot}} = \frac{1}{\mathrm{n}} + \sum_{\mathrm{i=1}}^{\mathrm{n}} \mathrm{MS_i} \tag{2}$$

$$\mathrm{MS_{tot}} = \frac{\sum_{\mathrm{i=1}}^{\mathrm{n}} \varphi_{\mathrm{i}}.\mathrm{MS_i}}{\sum_{\mathrm{i=1}}^{\mathrm{n}} \varphi_{\mathrm{i}}.\mathrm{MS_i}} \tag{3}$$

The second algorithm that used the image fusion technique mentioned in previous sections is the GS algorithm. The GS sharpening technique is used to enhance the multi-spectral spatial resolution bands by integrating both the high and low spatial image resolutions [48]. The GS simulates the high-resolution of the spectral band from the low-spatial resolution spectral band, making it the more accurate method. This is because it adopts the spectral responses of the sensor to calculate the high-resolution dataset. The low-spatial resolution spectral bands are adopted for simulating the UAV image bands. The stages of performing the GS algorithm are outlined below [49].

The first stage is to simulate the UAV image band (high-spatial-resolution band) from the WorldView-2 and/or the Sentinel-2 image (lower-spatial-resolution-spectral bands)

$$\mathrm{UAV_{sim}} = \sum_{k=1}^{n} W_k \, MS_k \tag{4}$$

where (W_k) represents a pixel weight, and (MS_k) represents a Multi-Spectral image.

The second is performing the GS transformation on the UAV image band, the third is replacing the UAV image band [a high-spatial-resolution] band with a first GS band. A four is employing the inverse of the GS transform from the UAV spectral bands. Figure 10 (a, b, c, d, e & F) shows the six levels of the fused images employing both the Brovey and GS algorithms on WorldView-2 and the Sentinel-2 satellite images.

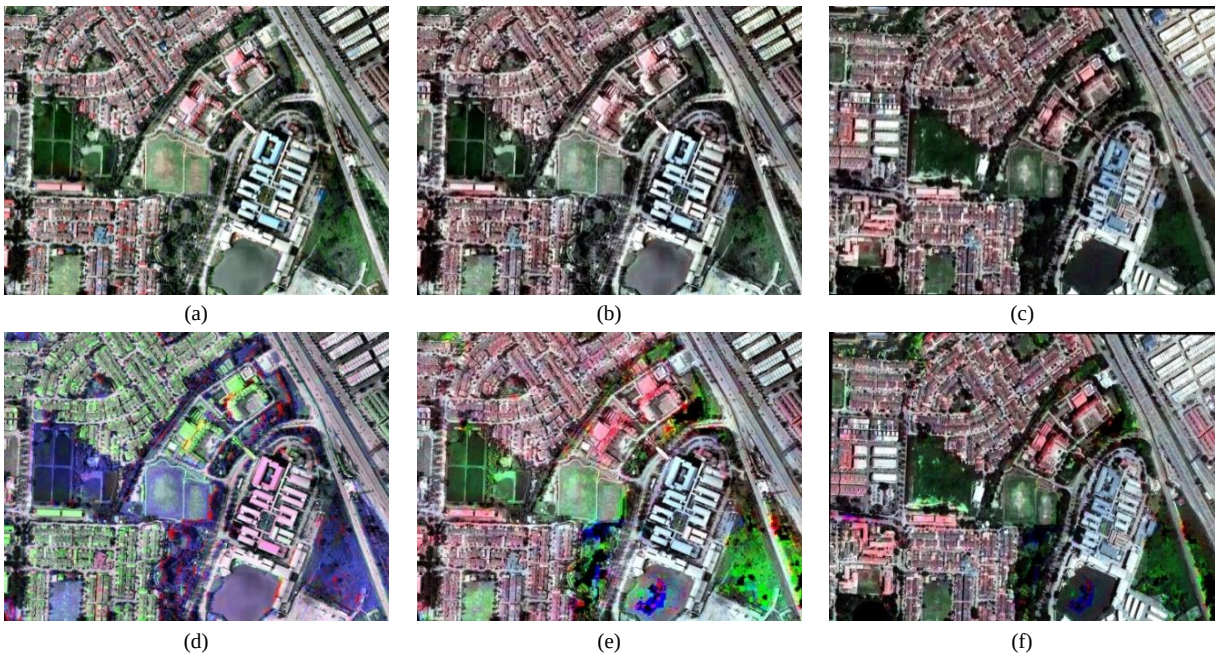

(a) (b) (c)

(d) (e) (f)

Figure 10. the fused image using the GS and Brovey spectral sharpening algorithms; (a) The GS spectral sharpening on UAV and WorldView-2 images, (b) The GS spectral sharpening on UAV and sentinel-2 images, (c) The GS spectral sharpening on WorldView-2 and Sentinel-2 images, (d) The Brovey spectral sharpening on UAV and WorldView-2 images, (e) The Brovey spectral sharpening on UAV and Sentinel-2 images, (f) The Brovey spectral sharpening on WorldView-2 and Sentinel-2 images.

5- Multi-Spectral Image Classifications

Many classification methods are adopted and applied for mapping and estimating the LU/LC patterns [50]. However, to perform imagery classification, the training and testing sites must be collected properly for every single class to orient the processing of the imagery classification and the assessment of outcome results [51]. The training samples will be compared to a corresponding region of interest (ROIs) group. The candidate sites group from the same groups and/or class may be spectrally similar [50]. For that, a wide range of candidate pixels should be sampled [46]. Ground-Truth References (GTR) must be observed to employ Pixel-Based Classifications (PBC). The GTR is usually selected by different techniques, such as using GPS devices in fieldwork or very high-resolution satellite or aerial images [52]. However, in the present study, Google Earth Pro was adopted for collecting the samples and testing sites using the Imagery-Visual-Interpretation-Process. The Google Earth Pro imagery has high spatial-resolution-quality imagery, and that must help for discovering the features in the Faculty of Engineering, UPM University. Eight classes were used to classify and produce the pattern of the LU/LC estimating map: Urban Roof-1, Urban Roof-2, Urban Roof-3, Urban Roof-4, Water, Grass, Roads, and Vegetation. Four urban roofs were selected in this study because the buildings in the study area have different roof materials. From the above datasets, 50% were presented as training samples. However, about 25% will be selected for the validation process. The training sites are used to train the classifier method. Both the sites of training and testing are equally distributed and collected into the imagery to guarantee accurate classification outputs. About 550 pixels were selected for each class of the eight classes for this study from each multi-spectral image of the UAV, WorldView-2, and Sentinel-2, and the six fused images using the GS and Brovey methods.

In this study, the ML method was applied to classify all nine images (three of them are multi-spectral images of UAV, WV-2, and Sentinel-2, and the other six are fused images). Using the ML algorithm for performing image classification in this study is efficient because it has a high efficiency when applied to multi-spectral images with High-Spatial-Resolution [53]. The default parameters of the ML were applied during the image classification process. The nine outputs of classified images were evaluated using the confusion matrix. The overall accuracy (OA) and the kappa coefficient (KC) are commonly adopted for result assessment [54]. The ML equations are indicated below:

$$OA = \frac{\sum_{i=1}^{c} n_{ij}}{n} \quad (4)$$

$$\text{kappa Coefficient} = \frac{\sum_{i=1}^{c} n_{ij} - \sum_{i=1}^{c} n_i + n - i}{n^2 - \sum_{i=1}^{c} n_i + n + i} \quad (5)$$

where {n} represents the total number of pixels, (n_{ij}) is equal to the total number of classified pixels, {n_i} is the instance number, and label {i} has been classified in the label {j}. The first stage of imagery classification is to conduct a supervised classification using the ML classifier to classify the multispectral images of the Faculty of Engineering and surrounding area in Serdang, Selangor, Malaysia, from the UAV, WorldView-2, and Sentinel-2, in order to generate the LU/LC pattern. The classification outcomes resulted in three different maps. All phases of imagery processing, analysis, classification, and accuracy assessment were conducted using the software called {Envi V. 5.3}. The confusion matrix was applied to assess the obtained results [55]. The evaluations of all classifications indicate that the classified Sentinel-2 image has the highest accuracy compared to the other images, with an overall accuracy of about 86.84% and a kappa coefficient value of 0.85, both visually and statistically. Figures 11-a to 11-c shows the maps estimating the LU/LC of the UAV, WorldView-2, and Sentinel-2 Multi-Spectral images. Table 2 presents the values of overall accuracy and kappa coefficients.

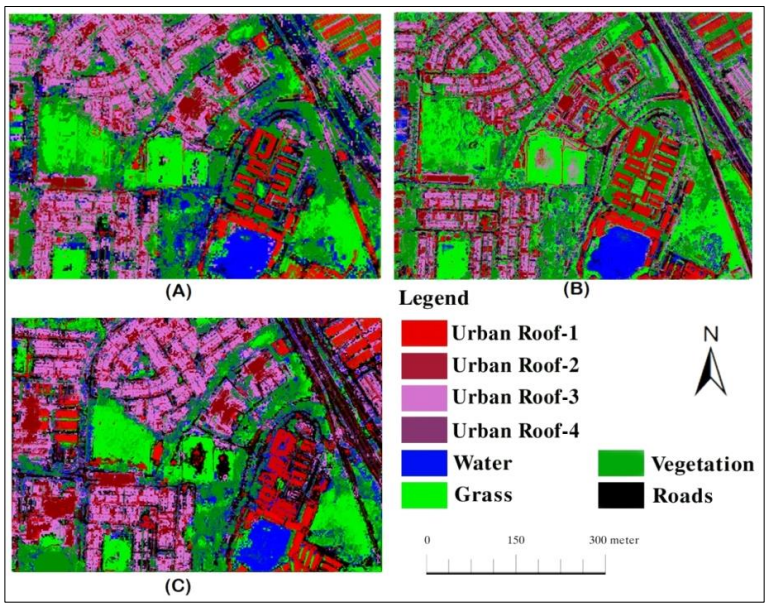

Figure 11. The maps of LU/LC using ML classifier, (A) classified UAV image, (B) classified WorldView-2 image, (C) classified Sentinel-2 imagery

Table 2. The overall-accuracies and kappa-coefficients values of all classified Multispectral Datasets

Classifier (ML)	Remote Sensing Images	Overall accuracy (%)	Kappa coefficient
Multispectral Datasets	UAV	76.49	0.69
	WorldView-2	85.10	0.80
	Sentinel-2	86.84	0.85

The statistical results indicate in Table 2 represent the OAs and the KCs of all the three classified Multispectral images (UAV, WorldView-2, and Sentinel-2) using the ML method. It is found that the highest OA and KC values were obtained from classified the Sentinel-2 multispectral images with the (OA and KC) values of about 86.84% and 0.85 respectively. However, the UAV classified image by ML has the lowest value of (OA and KC) about {76.49 %} and {0.69} respectively. Compared with the third classified WorldView-2 image. The classified WorldView-2 image record the second-highest (OA and KC) value with {85.10%} and {0.80} respectively.

6- Pan-Sharpening Images Classifications

6-1- Brovey Pan-Sharpening Image Classification

In this study, an image fusion method called the Brovey sharpening technique was employed on the three multi-spectral images (UAV, WorldView-2, and Sentinel-2) to produce three levels of fused images. Then, image classification using the ML classifier was applied to improve and enhance the estimating LU/LC, and to achieve the highest procedure accuracy. Furthermore, the eight classes mentioned in section 5 were classified for the three fused images. The confusion matrix was used to assess the outcomes and to calculate the overall accuracies (OAs) and kappa coefficients (KCs) of each level of fused images. A statistical comparison was made between the outcomes of the assessments. The pattern of the LU/LC maps is presented in Figure 12, and Table 3 provides the results of the assessments.

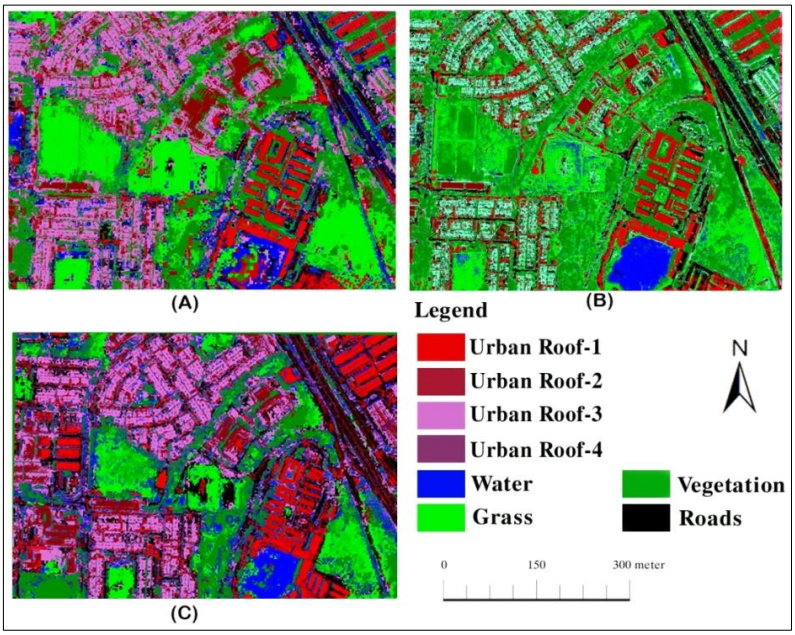

Figure 12. the three classified fused images using the ML classifier, (a) classified (UAV and Sentinel-2) fused images, (b) classified (UAV and WorldView-2) fused images, (c) classified (WorldView-2 and Sentinel-2) fused images

Table 3. the overall-accuracies and kappa-coefficients

Method	Remote Sensing Images	Overall-Accuracy (%)	Kappa-Coefficients
Brovey-Sharpening fused Image	UAV- Sentinel-2	85.75	0.82
	UAV -WorldView-2	76.68	0.71
	WV2-Sentinel-2	80.44	0.76

The statistical values indicated in Table 3 represent the results of the OA and the KC of all three levels of the classified fused images using the Brovey transformation method on the UAV, WorldView-2, and Sentinel-2 images with the ML technique as a classifier for this stage. It was found that the highest OA and KC values were obtained from the classified image of the integration and image fusion that was made between the UAV and the Sentinel-2 images. This fused image

obtained OA and KC values of about 85.75% and 0.82, respectively. However, the classified image by the ML approach on the fused image obtained from the fusion between the UAV and WorldView-2 images had the lowest OA and KC values of 76.68% and 0.71, respectively, when compared to the third classified fused image of WorldView-2 and Sentinel-2 images, which had the second-highest OA and KC values of 80.44% and 0.76, respectively.

6-2- The GS Pan-Sharpening Image Classification

The third image classification was performed on the fused images of the multispectral images (UAV, WorldView-2, and Sentinel-2) using an image fusion algorithm called the GS spectral-sharpening technique. The three fused images were classified by also employing the ML classifier to estimate the pattern of the LU/LC. Eight classes were selected to classify the three fused images, as the same as the previous classified images in the above sections. The obtained classified fused images were validated using the confusion-matrix approach. After that, a statistical comparison was conducted on all the obtained outcomes of the three classified fused images to determine which procedure has the most accurate results regarding others. The comparison shows that adopting the ML classifier on the fused images of integrating both WorldView-2 and Sentinel-2 images has the highest OA of about 88.47% with KC at about 0.85. Figure 13 and Table 4 illustrate the classified fused images using the GS method and the statistical results obtained.

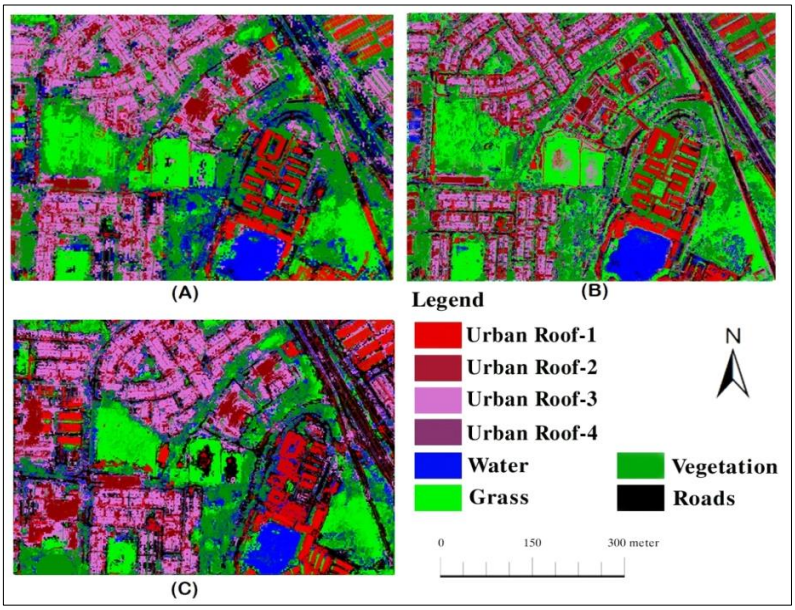

Figure 13. shows classified fused image using ML classifier, (a) classified UAV and Sentinel-2 fused images, (B) classified UAV and WorldView-2 fused images, (C) classified WorldView-2 and Sentinel-2 fused images

Table 4. the overall-accuracies and kappa-coefficients of all classifies

Method	Remote Sensing Images	Overall-Accuracy (%)	Kappa-Coefficient
GS-sharpening fused Image	UAV- Sentinel-2	83.69	0.79
	UAV - WorldView-2	84.49	0.81
	WorldView2-Sentinel-2	88.47	0.85

The statistical results indicated in Table 4 represent the OAs and KCs of all three classified fused images using the GS sharpening method on the multi-spectral UAV, WorldView-2, and Sentinel-2 images using the ML method as a classifier for this stage. It was found that the highest OA and KC values were achieved by integrating and fusing the images of both the WorldView-2 and Sentinel-2 satellite systems. This fused image had OA and KC values of 88.47% and 0.85, respectively. The classified image by the ML approach on the fused image obtained from the fusion between the UAV and Sentinel-2 images had the lowest OA and KC values, about 83.69% and 0.79%, respectively, when compared to the third classified fused image of UAV and WorldView-2 images, which recorded the second-highest OA and KC values at 84.49% and 0.81%, respectively.

7- Discussion

Figure 14 represents the results of all nine classified images using the ML classifier in terms of the OAs and KCs levels applied to the three multi-spectral images and the six fused images using the Brovey and GS sharpening techniques. The comparison in this study was made between the results of the nine generated LU/LC values, including

the OAs and KCs obtained from employing the confusion matrix to evaluate the results of the nine classified images. The most significant difficulty faced in this research was that all the adopted images had different spatial resolutions, with Sentinel-2 having the lowest spatial resolution of about 10m and UAV and WorldView-2 having the highest spatial resolutions of about 0.15m and 0.50m, respectively. Image fusion provides superior spatial details and information [55, 56], and different studies have applied imagery fusions between images with low and high spatial resolution [17–22]. The integration and fusion of images are conducted by combining the bands with high spatial information that have objects with high frequency with the multi-spectral information image that has objects with low frequency. By replacing the imagery of high-frequency objects with high-frequency imagery objects, the spatial resolution is improved without losing some of the spectral information [31]. Therefore, in this research, as indicated previously, imagery resampling was done using the bilinear method, and the resampling analysis was made using Envi software.

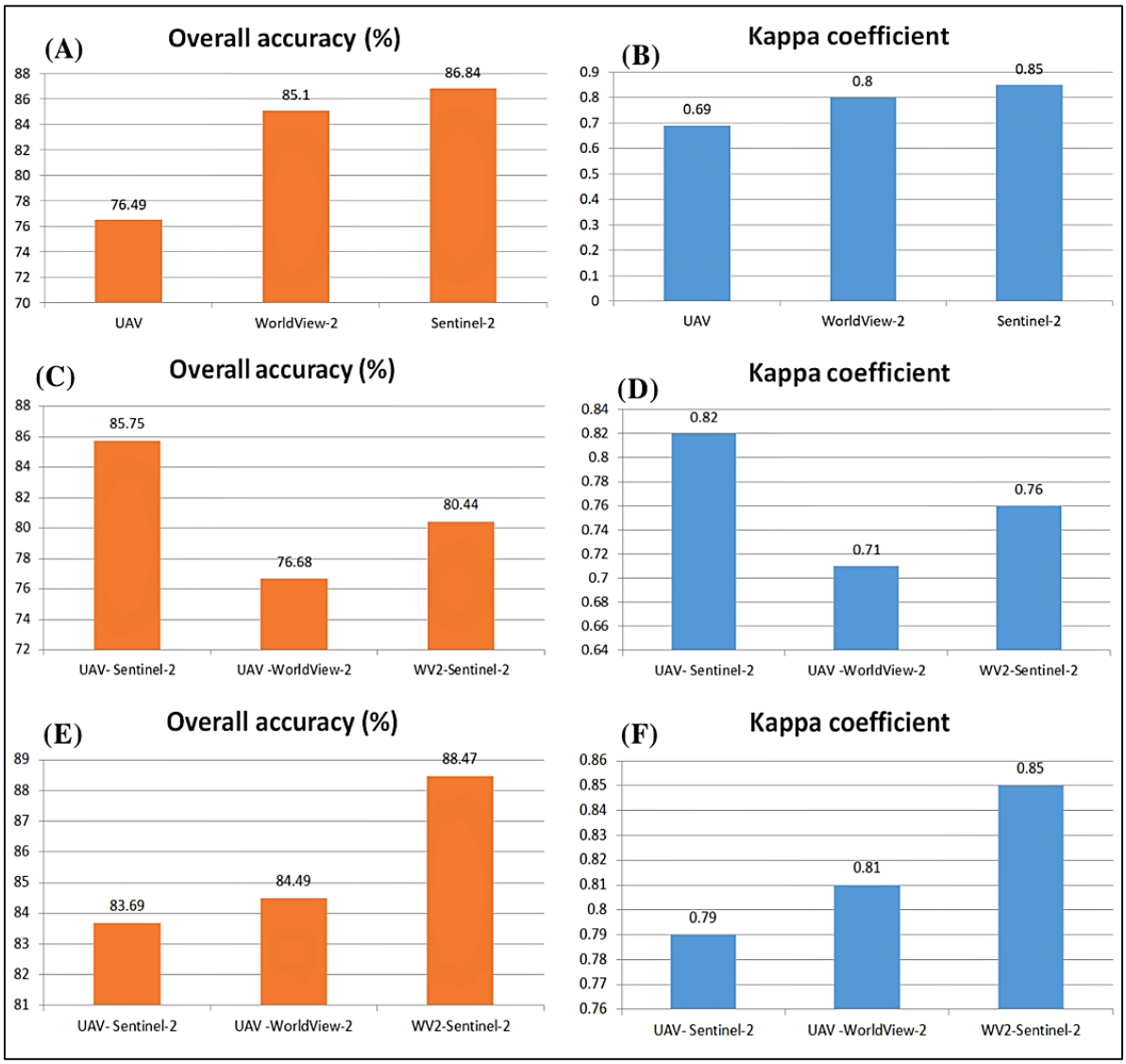

Figure 14. the classification accuracies assessment and Kappa coefficients of MS and fused data of Multi-spectral and fused data, (A & B) the Multi-spectral images results, (C) and (D) the Brovey fused images results, (E) and (F) the GS fused image results.

Figure 14 illustrates the OAs values obtained for all the classified images by the ML method from each classification of the three Multi-Spectral datasets and the six fused images. The ML method was found to be the best when applied to fuse the images of WorldView-2 and Sentinel-2 when integrated using the GS-sharpening technique. The classification outputs reflect that the highest accuracy is obtained from employing the ML technique. The ML method has an OA of about 88.47% with a KC value of 0.85. However, the other classified images fused by the Brovey method and/or multispectral classified images did not reach this level of accuracy and kappa coefficient. The objective of this research is to investigate and find out how to use different high-spatial-resolution imagery to enhance the accuracy of creating an accurate map of the LU/LC. Therefore, based on all the outcomes obtained in this study, it can be seen that the optimal method to obtain the highest outputs to create the LU/LC map is by employing the imagery integration of WorldView-2 and Sentinel-2 using GS-spectral-sharpening and classification with the ML method.

8- Conclusion

This study analyzes the adoption of different aerial and satellite images with varying spatial resolutions (UAV, WorldView-2, and Sentinel-2) to obtain the most accurate procedure for creating a LU/LC map of the Faculty of Engineering at UPM University and its surrounding area in Serdang, Selangor, Malaysia. A statistical comparison is performed between the results of the three multi-spectral classified images using the ML method and the other six classified fused images using the GS and Brovey approaches. The confusion matrix is adopted for results assessment. The results show that the ML approach using the GS and Brovey methods provides the highest accuracy compared to all other classified fused and multispectral images. The fused classified image with the GS method and the ML approach between WorldView-2 and Sentinel-2 produces the highest outcome among all classified images, with an OA value of 88.47% and a kappa coefficient of 0.85. However, the multispectral UAV classified image by the ML method obtains the lowest accurate result with an OA of 76.49% and a KC of 0.69. Additionally, the classification of the multispectral image of the Sentinel-2 satellite image obtained the second-most accurate result among the nine classified images, with an OA of about 86.84% and a KC of about 0.85. In future work, other approaches and methods such as object-oriented, feature extraction, and image segmentation should be tested and statistically compared with the pixel-based classifiers. The research outcomes will contribute to the academic field and improve the present study for use with different datasets, applications, sources, and sites.

9- Declarations

9-1- Author Contributions

Conceptualization, H.D., H.S.J., and N.A.A.; methodology, H.D. H.S.J., and N.A.A.; software, H.D. and N.A.A.; validation, H.D. and N.A.A.; investigation, H.D. and N.A.A.; data curation, H.D., H.S.J., and N.A.A.; writing—original draft preparation, H.D., H.S.J., and N.A.A.; visualization, N.A.A.; project administration, N.A.A. All authors have read and agreed to the published version of the manuscript.

9-2- Data Availability Statement

Data available on request due to restrictions, the data presented in this study are available on request from the corresponding author. The data are not publicly available due to it relate to AL-Qasim Green University.

9-3- Funding and Acknowledgements

The authors also would like to express their thankfulness to the AL-Qasim Green University, College (Iraq), Lulea University of Technology (Sweden) for the support provided to accomplish this study.

9-4- Institutional Review Board Statement

Not applicable.

9-5- Informed Consent Statement

Not applicable.

9-6- Conflicts of Interest

The authors declare that there is no conflict of interest regarding the publication of this manuscript. In addition, the ethical issues, including plagiarism, informed consent, misconduct, data fabrication and/or falsification, double publication and/or submission, and redundancies have been completely observed by the authors.

10- References

[1] Otukei, J. R., Blaschke, T., & Collins, M. (2015). Fusion of TerraSAR-x and Landsat ETM+ data for protected area mapping in Uganda. International Journal of Applied Earth Observation and Geoinformation, 38, 99–104. doi:10.1016/j.jag.2014.12.012.

[2] Huiyong Sang, Jixian Zhang, Liang Zhai, Chengji Qiu, & Xiaoxia Sun. (2014). Analysis of RapidEye imagery for agricultural land cover and land use mapping. 2014 Third International Workshop on Earth Observation and Remote Sensing Applications (EORSA). doi:10.1109/eorsa.2014.6927914.

[3] Dibs, H., Idrees, M. O., Saeidi, V., & Mansor, S. (2016). Automatic keypoints extraction from UAV image with refine and improved scale invariant features transform (RI-SIFT). International Journal of Geoinformatics, 12(3), 31–58.

[4] Fahad, K. H., Hussein, S., & Dibs, H. (2020). Spatial-Temporal Analysis of Land Use and Land Cover Change Detection Using Remote Sensing and GIS Techniques. IOP Conference Series: Materials Science and Engineering, 671(1), 012046. doi:10.1088/1757-899x/671/1/012046.

[5] Dibs, H., Hasab, H. A., Mahmoud, A. S., & Al-Ansari, N. (2021). Fusion Methods and Multi-classifiers to Improve Land Cover Estimation Using Remote Sensing Analysis. Geotechnical and Geological Engineering, 39(8), 5825–5842. doi:10.1007/s10706-021-01869-x.

[6] Gevana, D., Camacho, L., Carandang, A., Camacho, S., & Im, S. (2015). Land use characterization and change detection of a small mangrove area in Banacon Island, Bohol, Philippines using a maximum likelihood classification method. Forest Science and Technology, 11(4), 197–205. doi:10.1080/21580103.2014.996611.

[7] Dibs, H., Mansor, S., Ahmad, N., Pradhan, B., & Al-Ansari, N. (2020). Automatic Fast and Robust Technique to Refine Extracted SIFT Key Points for Remote Sensing Images. Journal of Civil Engineering and Architecture, 14(6), 339-350. doi:10.17265/1934-7359/2020.06.005.

[8] Chasmer, L., Hopkinson, C., Veness, T., Quinton, W., & Baltzer, J. (2014). A decision-tree classification for low-lying complex land cover types within the zone of discontinuous permafrost. Remote Sensing of Environment, 143, 73–84. doi:10.1016/j.rse.2013.12.016.

[9] Dibs, H., Mansor, S., Ahmad, N., & Pradhan, B. (2015). Band-to-band registration model for near-equatorial Earth observation satellite images with the use of automatic control point extraction. International Journal of Remote Sensing, 36(8), 2184–2200. doi:10.1080/01431161.2015.1034891.

[10] Löw, F., Conrad, C., & Michel, U. (2015). Decision fusion and non-parametric classifiers for land use mapping using multi-temporal RapidEye data. ISPRS Journal of Photogrammetry and Remote Sensing, 108, 191–204. doi:10.1016/j.isprsjprs.2015.07.001.

[11] Cavur, M., Duzgun, H. S., Kemec, S., & Demirkan, D. C. (2019). Land Use and Land Cover Classification of Sentinel 2-A: St Petersburg Case Study. The International Archives of the Photogrammetry, Remote Sensing and Spatial Information Sciences, XLII-1/W2, 13–16. doi:10.5194/isprs-archives-xlii-1-w2-13-2019.

[12] Kadhim, N., Ismael, N. T., & Kadhim, N. M. (2022). Urban Landscape Fragmentation as an Indicator of Urban Expansion Using Sentinel-2 Imageries. Civil Engineering Journal, 8(9), 1799-1814. doi:10.28991/CEJ-2022-08-09-04.

[13] Dibs, H., AL-Hedny, S., & Abed Karkoosh, H. S. (2018). Extracting detailed buildings 3D model with using high resolution satellite imagery by remote sensing and GIS analysis; Al-Qasim Green University a case study. International Journal of Civil Engineering and Technology, 9(7), 1097–1108.

[14] Mann, R., & Gupta, A. (2022). Temporal Trends of Rainfall and Temperature over Two Sub-Divisions of Western Ghats. HighTech and Innovation Journal, 3, 28-42. doi:10.28991/HIJ-SP2022-03-03.

[15] Ghahremani, M., & Ghassemian, H. (2016). A compressed-sensing-based pan-sharpening method for spectral distortion reduction. IEEE Transactions on Geoscience and Remote Sensing, 54(4), 2194–2206. doi:10.1109/TGRS.2015.2497309.

[16] Zhang, L., Gong, Z., Wang, Q., Jin, D., & Wang, X. (2019). Wetland mapping of Yellow River Delta wetlands based on multi-feature optimization of Sentinel-2 images. Journal of Remote Sensing, 23(2), 313–326. doi:10.11834/jrs.20198083.

[17] Padmanaban, R., Bhowmik, A. K., & Cabral, P. (2019). Satellite image fusion to detect changing surface permeability and emerging urban heat islands in a fast-growing city. PLoS ONE, 14(1), 208949. doi:10.1371/journal.pone.0208949.

[18] Wang, L., Chang, Q., Yang, J., Zhang, X., & Li, F. (2018). Estimation of paddy rice leaf area index using machine learning methods based on hyperspectral data from multi-year experiments. PLoS ONE, 13(12), 207624. doi:10.1371/journal.pone.0207624.

[19] Ma, Y., Fang, S., Peng, Y., Gong, Y., & Wang, D. (2019). Remote estimation of biomass in winter oilseed rape (Brassica napus L.) using canopy hyperspectral data at different growth stages. Applied Sciences (Switzerland), 9(3), 545. doi:10.3390/app9030545.

[20] Hashim, F., Dibs, H., & Jaber, H. S. (2021). Applying Support Vector Machine Algorithm on Multispectral Remotely sensed satellite image for Geospatial Analysis. Journal of Physics: Conference Series, 1963(1). doi:10.1088/1742-6596/1963/1/012110.

[21] Dibs, H., Hasab, H. A., Jaber, H. S., & Al-Ansari, N. (2022). Automatic feature extraction and matching modelling for highly noise near-equatorial satellite images. Innovative Infrastructure Solutions, 7(1), 1–14. doi:10.1007/s41062-021-00598-7.

[22] Xu, B., Liang, C., Chai, D., Shi, W., & Sun, G. (2014). Inversion of natural grassland productivity from remote sensor imagery in Zulihe River Basin. Arid Zone Research, 31, 1147-1152.

[23] Wang, W., Zhang, X., Zhao, Y., & Wang, S. (2017). Cotton extraction method of integrated multi-features based on multitemporal Landsat 8 images. Yaogan Xuebao/Journal of Remote Sensing, 21(1), 115–124. doi:10.11834/jrs.20175317.

[24] Wang, X., & Chen, D. (2018). Interannual variability of GNDVI and its relationship with altitudinal in the Three-River Headwater Region. Journal of Ecology and Environmental Sciences, 27, 1411-1416.

[25] Sun, C., Bian, Y., Zhou, T., & Pan, J. (2019). Using of multi-source and multi-temporal remote sensing data improves crop-type mapping in the subtropical agriculture region. Sensors (Switzerland), 19(10), 2401. doi:10.3390/s19102401.

[26] Dibs, H., Mansor, S., Ahmad, N., & Al-Ansari, N. (2022). Geometric Correction Analysis of Highly Distortion of Near Equatorial Satellite Images Using Remote Sensing and Digital Image Processing Techniques. Engineering, 14(01), 1–8. doi:10.4236/eng.2022.141001.

[27] Otazu, X., González-Audícana, M., Fors, O., & Núñez, J. (2005). Introduction of Sensor Spectral Response into Image Fusion Methods. Application to Wavelet-Based Methods. IEEE Transactions on Geoscience and Remote Sensing, 43(10), 2376–2385. doi:10.1109/TGRS.2005.856106.

[28] Ibarrola-Ulzurrun, E., Gonzalo-Martin, C., Marcello-Ruiz, J., Garcia-Pedrero, A., & Rodriguez-Esparragon, D. (2017). Fusion of high resolution multispectral imagery in vulnerable coastal and land ecosystems. Sensors (Switzerland), 17(2), 228. doi:10.3390/s17020228.

[29] Kavzoglu, T., & Tonbul, H. (2018). An experimental comparison of multi-resolution segmentation, SLIC and k-means clustering for object-based classification of VHR imagery. International Journal of Remote Sensing, 39(18), 6020–6036. doi:10.1080/01431161.2018.1506592.

[30] Li, S., Kang, X., Fang, L., Hu, J., & Yin, H. (2017). Pixel-level image fusion: A survey of the state of the art. Information Fusion, 33, 100–112. doi:10.1016/j.inffus.2016.05.004.

[31] Guo, Q., Ehlers, M., Wang, Q., Pohl, C., Hornberg, S., & Li, A. (2017). Ehlers pan-sharpening performance enhancement using HCS transform for n-band data sets. International Journal of Remote Sensing, 38(17), 4974–5002. doi:10.1080/01431161.2017.1320448.

[32] Laben, C. A., & Brower, B. V. (2000). U.S. Patent No. 6,011,875. Washington, DC: U.S. Patent and Trademark Office, Alexandria, United States

[33] Gonzalez-Audicana, M., Saleta, J. L., Catalan, R. G., & Garcia, R. (2004). Fusion of multispectral and panchromatic images using improved IHS and PCA mergers based on wavelet decomposition. IEEE Transactions on Geoscience and Remote Sensing, 42(6), 1291–1299. doi:10.1109/tgrs.2004.825593.

[34] Pradhan, P. S., King, R. L., Younan, N. H., & Holcomb, D. W. (2006). Estimation of the number of decomposition levels for a wavelet-based multiresolution multisensor image fusion. IEEE Transactions on Geoscience and Remote Sensing, 44(12), 3674–3686. doi:10.1109/TGRS.2006.881758.

[35] Shah, V. P., Younan, N. H., & King, R. L. (2008). An efficient pan-sharpening method via a combined adaptive PCA approach and contourlets. IEEE Transactions on Geoscience and Remote Sensing, 46(5), 1323–1335. doi:10.1109/TGRS.2008.916211.

[36] Nencini, F., Garzelli, A., Baronti, S., & Alparone, L. (2007). Remote sensing image fusion using the curvelet transform. Information Fusion, 8(2), 143–156. doi:10.1016/j.inffus.2006.02.001.

[37] Aiazzi, B., Alparone, L., Baronti, S., Carlà, R., Garzelli, A., & Santurri, L. (2017). Sensitivity of Pansharpening Methods to Temporal and Instrumental Changes Between Multispectral and Panchromatic Data Sets. IEEE Transactions on Geoscience and Remote Sensing, 55(1), 308–319. doi:10.1109/TGRS.2016.2606324.

[38] Meng, X., Li, J., Shen, H., Zhang, L., & Zhang, H. (2016). Pansharpening with a guided filter based on three-layer decomposition. Sensors (Switzerland), 16(7), 1068. doi:10.3390/s16071068.

[39] Li, S., & Yang, B. (2011). A new pan-sharpening method using a compressed sensing technique. IEEE Transactions on Geoscience and Remote Sensing, 49(2), 738–746. doi:10.1109/TGRS.2010.2067219.

[40] Huang, B., Song, H., Cui, H., Peng, J., & Xu, Z. (2014). Spatial and spectral image fusion using sparse matrix factorization. IEEE Transactions on Geoscience and Remote Sensing, 52(3), 1693–1704. doi:10.1109/TGRS.2013.2253612.

[41] Imani, M., & Ghassemian, H. (2017). Pansharpening optimisation using multiresolution analysis and sparse representation. International Journal of Image and Data Fusion, 8(3), 270–292. doi:10.1080/19479832.2017.1334713.

[42] Maglione, P. (2016). Very High Resolution Optical Satellites: An Overview of the Most Commonly used. American Journal of Applied Sciences, 13(1), 91–99. doi:10.3844/ajassp.2016.91.

[43] Vrabel, J. (1996). Multispectral imagery band sharpening study. Photogrammetric engineering and remote sensing, 62(9), 1075-1084.

[44] Saroglu, E., Bektas, F., Musaoglu, N., & Goksel, C. (2004). Fusion of multisensor remote sensing data: assessing the quality of resulting images. International Archives of the Photogrammetry, Remote Sensing and Spatial Information Sciences, 35, 575-579.

[45] Gharbia, R., El Baz, A. H., Hassanien, A. E., & Tolba, M. F. (2014). Remote Sensing Image Fusion Approach Based on Brovey and Wavelets Transforms. Advances in Intelligent Systems and Computing, 303, 311–321. doi:10.1007/978-3-319-08156-4_31.

[46] Mhangara, P., Mapurisa, W., & Mudau, N. (2020). Comparison of image fusion techniques using Satellite pour l'Observation de la terre (SPOT) 6 satellite imagery. Applied Sciences (Switzerland), 10(5), 1881. doi:10.3390/app10051881.

[47] Johnson, B. (2014). Effects of pansharpening on vegetation indices. ISPRS International Journal of Geo-Information, 3(2), 507–522. doi:10.3390/ijgi3020507.

[48] Pohl, C., & Van Genderen, J. L. (1998). Review article Multisensor image fusion in remote sensing: Concepts, methods and applications. International Journal of Remote Sensing, 19(5), 823–854. doi:10.1080/014311698215748.

[49] Maurer, T. (2013). How to pan-sharpen images using the gram-schmidt pan-sharpen method–A recipe. International Archives of the Photogrammetry, Remote Sensing and Spatial Information Sciences, XL-1/W1, ISPRS Hannover Workshop, 21 – 24 May, 2013, Hannover, Germany

[50] Ban, Y., Hu, H., & Rangel, I. M. (2010). Fusion of Quickbird MS and RADARSAT SAR data for urban land-cover mapping: Object-based and knowledge-based approach. International Journal of Remote Sensing, 31(6), 1391–1410. doi:10.1080/01431160903475415.

[51] Dibs, H., Idrees, M. O., Saeidi, V., & Mansor, S. (2016). Automatic keypoints extraction from UAV image with refine and improved scale invariant features transform (RI-SIFT). International Journal of Geoinformatics, 12(3), 51-58.

[52] Lu, D., Li, G., Moran, E., Dutra, L., & Batistella, M. (2011). A comparison of multisensor integration methods for land cover classification in the Brazilian Amazon. GIScience and Remote Sensing, 48(3), 345–370. doi:10.2747/1548-1603.48.3.345.

[53] Taubenböck, H., Felbier, A., Esch, T., Roth, A., & Dech, S. (2012). Pixel-based classification algorithm for mapping urban footprints from radar data: A case study for RADARSAT-2. Canadian Journal of Remote Sensing, 38(3), 211–222. doi:10.5589/m11-061.

[54] Nishii, R., & Tanaka, S. (1999). Accuracy and inaccuracy assessments in land-cover classification. IEEE Transactions on Geoscience and Remote Sensing, 37(1), 491–498. doi:10.1109/36.739098.

[55] Jing, L., & Cheng, Q. (2009). Two improvement schemes of PAN modulation fusion methods for spectral distortion minimization. International Journal of Remote Sensing, 30(8), 2119–2131. doi:10.1080/01431160802549260.

[56] Garzelli, A., & Nencini, F. (2005). Interband structure modeling for Pan-sharpening of very high-resolution multispectral images. Information Fusion, 6(3), 213–224. doi:10.1016/j.inffus.2004.06.008.